Article

Multimaterial cryogenic printing of three-dimensional soft hydrogel machines

Jinhao Li [1], Jie Cao[2], Rong Bian[1], Rongtai Wan[2], Xiangyang Zhu [1,3] ✉, Baoyang Lu [2] ✉ & Guoying Gu [1,3] ✉

Hydrogel-based soft machines are promising in diverse applications, such as biomedical electronics and soft robotics. However, current fabrication techniques generally struggle to construct multimaterial three-dimensional hydrogel architectures for soft machines and robots, owing to the inherent hydrogel softness from the low-density polymer network nature. Herein, we present a multimaterial cryogenic printing (MCP) technique that can fabricate sophisticated soft hydrogel machines with accurate yet complex architectures and robust multimaterial interfaces. Our MCP technique harnesses a universal all-in-cryogenic solvent phase transition strategy, involving instant ink solidification followed by in-situ synchronous solvent melting and cross-linking. We, therefore, can facilely fabricate various multimaterial 3D hydrogel structures with high aspect ratio complex geometries (overhanging, thin-walled, and hollow) in high fidelity. Using this approach, we design and manufacture all-printed all-hydrogel soft machines with versatile functions, such as self-sensing biomimetic heart valves with leaflet-status perception and untethered multimode turbine robots capable of in-tube blockage removal and transportation.

Introducing multimaterial three-dimensional hydrogel structures into soft machines and robots is attracting increasing attention to mimic[1–3], coorporate[4–6], and substitute[7,8] natural systems. Towards this goal, many interesting works have been reported, generally focusing on ink-by-ink solute regulation to cater to conventional solute-triggered formation mechanisms, such as polymerization[9–11], sol-gel transition[12,13], self-assembly[14], and phase separation[15,16]. Despite these recent advances, existing techniques are still struggling to precisely fabricate multimaterial 3D-architectured hydrogels for soft robots and machines. This difficulty mainly arises from the low-density polymer network nature of hydrogel materials and weak yet inconsistent mechanics across multiple hydrogels (Fig. 1a)[17–20]. Alternatively, solvents (mostly water) that carry hydrogel networks throughout the production cycle are expected to revolutionize multimaterial hydrogel fabrication. Rapid freezing prototyping deposits and freezes aqueous inks on demand to provide structure rigidity for dimension-raising manufacturing[21–23]. For example, Rubinsky et al. have pioneered cryo-printed bioactive 3D scaffolds and systematically indicated temperature-controlled water crystallization benefiting hydrogel-based tissue engineering[24–27]. Nevertheless, it remains technically challenging to accurately structuralize multiple hydrogel networks (Supplementary Fig. 1), impeding the integrated manufacturing of soft hydrogel machines.

Herein, we present a MCP fabrication paradigm for multimaterial 3D-architectured hydrogels. By proposing an all-in-cryogenic solvent phase transition strategy (Fig. 1b), our MCP paradigm facilitates multiple hydrogel materials into geometrically complex 3D structures with high aspect ratios. This integrated manufacturing capability demonstrates all-printed all-hydrogel soft machines with versatile functions, such as self-sensing

[1]Robotics Institute and State Key Laboratory of Mechanical System and Vibration, School of Mechanical Engineering, Shanghai Jiao Tong University, Shanghai, China. [2]Jiangxi Provincial Key Laboratory of Flexible Electronics, Flexible Electronics Innovation Institute, Jiangxi Science and Technology Normal University, Nanchang, China. [3]Meta Robotics Institute, Shanghai Jiao Tong University, Shanghai, China. ✉e-mail: mexyzhu@sjtu.edu.cn; luby@jxstnu.edu.cn; guguoying@sjtu.edu.cn
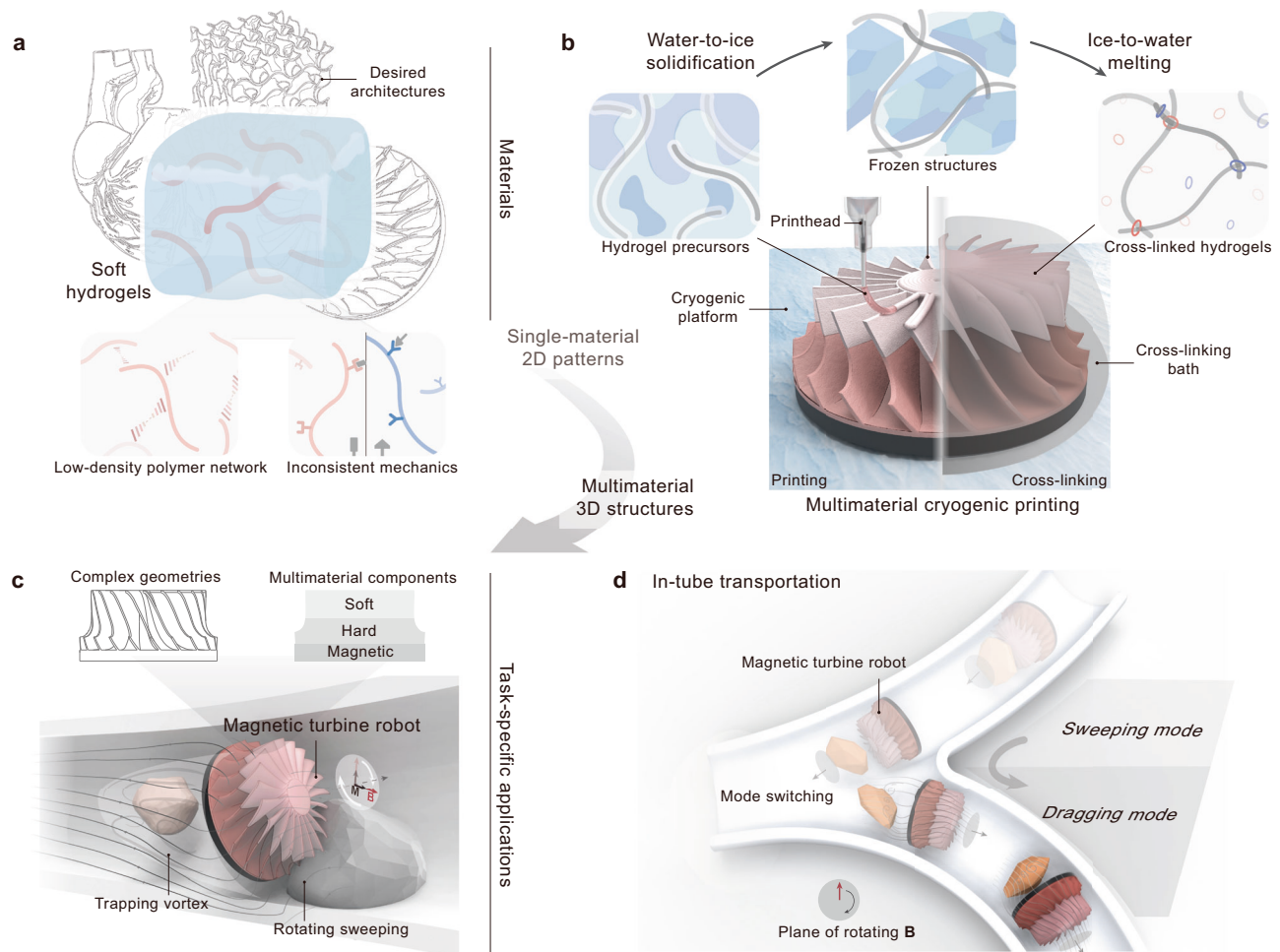
Fig. 1 | Multimaterial cryogenic printing technique for soft hydrogel machines.
a Schematic diagram of the mismatch between desired structure designs and soft formless hydrogels, owing to weak and inconsistent interfacial mechanics across low-density polymer networks. **b** Schematic diagram of proposed multimaterial cryogenic printing technique by all-in-cryogenic solvent phase transition, involving cryogenic printing and cryogenic cross-linking procedures. **c** Schematic diagram of an untethered multimode turbine robot actuated by a rotating magnetic field: sweeping with soft-hard composite blades and dragging by generating a trapping vortex. **d** Schematic diagram of a turbine robot capable of transporting cargo through an underwater Y-shape tube by steering its rotational axis to switch between sweeping and dragging modes. **M** in-plane magnetization, **B** magnetic field.

biomimetic heart valves with leaflet-status perception and untethered magnetic turbine robots with twenty soft-hard composite blades (Fig. 1c). This turbine robot with varying locomotion modes (sweeping and dragging) further brings the capabilities for complicated in-tube blockage removal and transportation (Fig. 1d).

Results

Multimaterial cryogenic printing

Our MCP technique utilizes an all-in-cryogenic solvent phase transition strategy to fabricate multimaterial 3D-architectured hydrogels through two steps (Fig. 1b). The first step uses instant phase transition of water into ice to physically lock down the molecular configuration of hydrogel precursors (Fig. 2a). By introducing a cryogenic platform into the direct-ink-writing (DIW) 3D printing system (Supplementary Fig. 2), we can rapidly solidify a variety of aqueous hydrogel inks into frozen 3D structures at a low-temperature range from −30 to −10 °C. The second step exploits reverse ice-to-water phase transition to initiate the chemical cross-linking of frozen hydrogel molecular networks at the melting ice-water interface (Fig. 2f). To this end, we design a cross-linker-containing bath with low freezing points to construct a cryogenic ice-water mixed system (typically at −5 °C) for cross-linking the immersed frozen

structures (Supplementary Fig. 3). The diffusion of cross-linkers at the ice-water interface initiates synchronized ice melting and cross-linking reactions to transit a pre-locked molecular configuration into polymer networks, maintaining the structure rigidity[28,29]. Such an all-in-cryogenic solvent phase transition strategy can effectively achieve free-standing yet complicated 3D-printed hydrogel architectures in high shape fidelity. The as-developed MCP technique is theoretically universal to all extrudable aqueous hydrogel inks, substantially enriching the printable material library and geometrical complexity in three dimensions to create desired hydrogel-based soft machines.

Kinetic validation and modeling

Next, we monitor the kinetics of our MCP technique by in-situ microscope imaging of the cryogenic printing process. Firstly, we can clearly observe a crystallization frontline in the just-extruded filaments by water solidification to form a hard ice shell (Fig. 2b and Supplementary Video 1). Such a surface ice crystallization behavior provides instant solidification within 0.5 s, facilitating the reliable construction of seamless line-by-line interfaces (Supplementary Fig. 4). In scanning electron microscope (SEM) images (Fig. 2b and Supplementary Fig. 5), the cryogenically printed filaments exhibit uniform micropores with a 0.8 μm-thick polymer shell as the outer surface, while room-
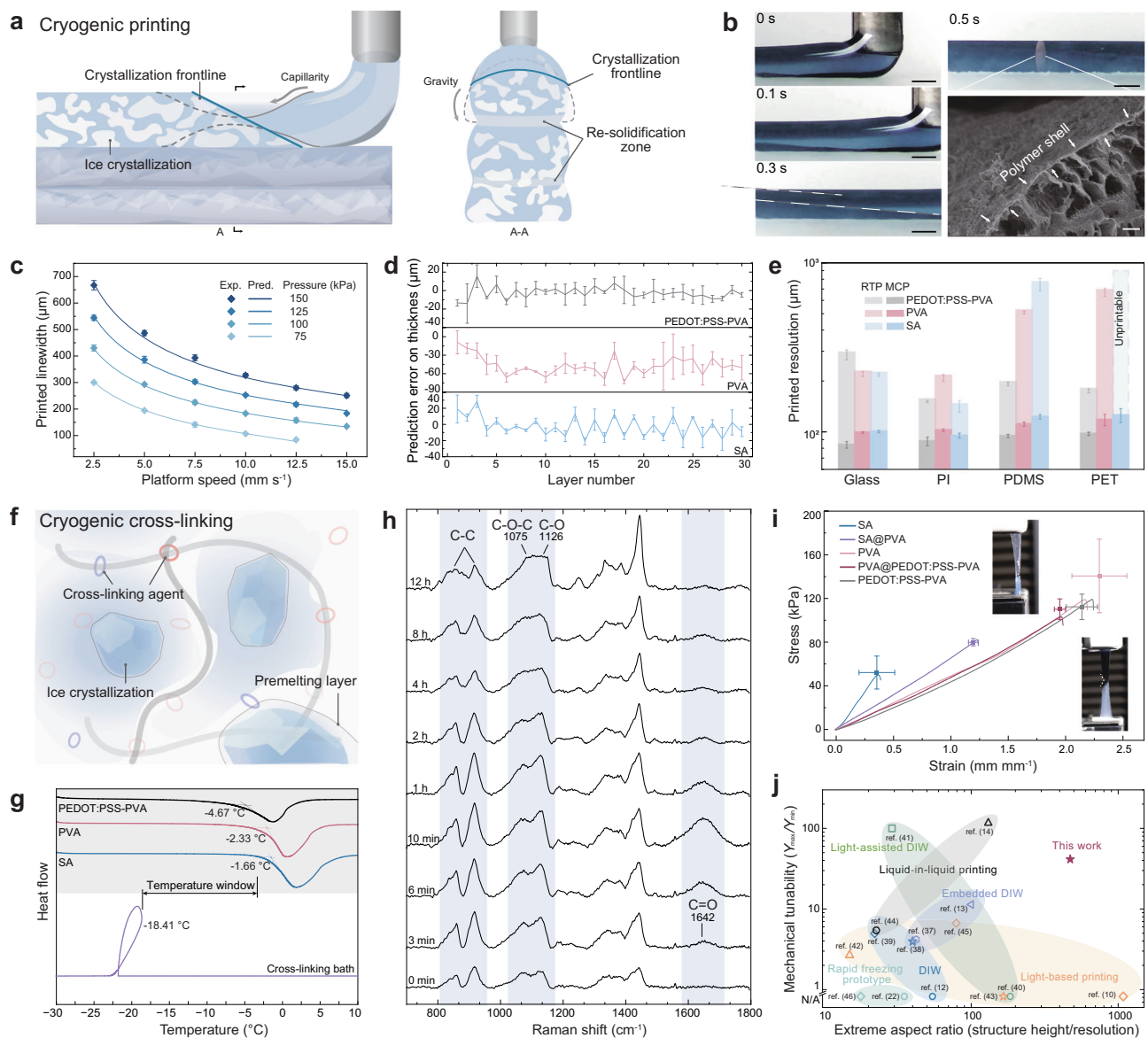
Fig. 2 | Characterizations of multimaterial cryogenic printing technique. **a**–**e** Cryogenic printing: **a** Schematic diagram of printing high-resolution 3D structures enabled by instant solidification against capillarity- and gravity-driven instability. **b** In-situ observations of instant ink-solvent solidification and SEM cross-sectional image of printed filamentary hydrogels. Scale bars, 200 μm (optical images), 5 μm (SEM image). **c** The kinetic predictions on printed linewidth compared to experimental measurements under varying platform moving speeds and extrusion pressures. Pred. prediction. **d** The kinetic prediction errors on the layer thickness of thin walls compared to experimental measurements, by using multiple hydrogel inks like PEDOT:PSS-PVA, PVA, and SA. **e** The generalized resolution improvement on multiple hydrogel choices and printing substrates by using cryogenic printing. RTP room-temperature printing, PI polyimide, PDMS poly-dimethylsiloxane, PET polyethylene terephthalate. The comparisons use the same 32 G nozzles for printing hydrogel inks. **f**–**j** Cryogenic cross-linking: **f** Schematic diagram of cryogenic cross-linking reactions at the synchronously melting ice-water interfaces. **g** Differential scanning calorimetry (DSC) curves of typical hydrogel inks and cross-linking baths. The cross-linking process is designed to react within the temperature window between the melting temperature of frozen inks and the solidification temperature of baths. **h** Raman spectra of frozen PVA structures after immersing in cross-linking baths show the reaction process at −5 °C. **i** Uniaxial tensile tests of the printed multimaterial hydrogel samples and corresponding composed single-material samples. Typical snapshots of the heterogeneous samples are inserted within this panel. @, heterogeneous sample. **j** Printing performance comparisons on mechanical tunability (the ratio of maximum and minimum Young's modulus, Y_{max}/Y_{min}) and extreme aspect ratio (the ratio of structural height to resolution) with existing approaches. DIW direct-ink-writing. Error bars indicate one standard deviation from the mean over three samples.

temperature printed samples show a hierarchical porous morphology. The formation of the polymer shell can be attributed to the surface ice crystallization behavior, which results from the phase transition of supercooling inks[30,31]. To guide and interpret the above cryogenic printing kinetics, we develop a theoretical model to express the relationship of the printed linewidth d and the extrusion flow Q by considering bow-shape cross-section and in-flight stretching, as follows (Supplementary Fig. 6, See Supplementary Note 1 for

detailed derivation):

$$Q = \left(\frac{\pi}{4\sin\theta} - \frac{\theta\pi}{180} + \sin 2\theta \right) d^2 + \frac{\pi R^2 v}{\sqrt{\left(\frac{\tau_y R}{2\sigma}\right)^4 - 1}} \quad (1)$$

As shown in Fig. 2c, the developed model can accurately predict experimentally printed linewidth under varying printing parameters

(average error less than 1.67%). We further verify that such a model is also available for universal geometrical predictions on multimaterial 3D structures (Fig. 2d).

For the cryogenic cross-linking of the printed structures, the designed special cross-linking baths with low freezing points (e.g., −18 °C) synchronize ice melting and chemical cross-linking reactions (Fig. 2f, g). The ice-water mixed system allows cross-linkers in liquid baths to diffuse into the premelting layer of immersed frozen printed structures[32,33]. This cryogenic ice-to-water phase transition extends the melting time scale (from seconds to hours) for chemical cross-linking at the ice-water interface. Such a mechanism macroscopically behaves as synchronous ice melting and hydrogel cross-linking gradually from the outside in (Supplementary Fig. 3). Furthermore, we in-situ monitor the cryogenic cross-linking kinetics by Raman spectroscopy taking glutaraldehyde (GA) cross-linked poly(vinyl alcohol) (PVA) as an example (Fig. 2h). At first, the peak at $1642 \, cm^{-1}$ corresponds to the C=O stretching vibration of GA, representing the initial diffusion of cross-linkers into frozen printed structures. By increasing the immersion time, the peaks at $1075 \, cm^{-1}$ (the symmetric stretching of C-O-C bonds) and $1126 \, cm^{-1}$ (the stretching of C-O bonds) of the printed PVA hydrogels gradually become stronger and notably broadened, indicating the occurrence of the aldol condensation reaction[34]. To further analyze the kinetic results, we evaluate varying parameters influencing the cross-linking density and equilibrium swelling of the resultant hydrogels by polymer content φ, such as cross-linking time, temperature, and cross-linker/catalyst concentration (Supplementary Fig. 7, 8 and Supplementary Note 2, 3). These parameters enable fine tunability on the shape fidelity and mechanical properties of printed hydrogel structures.

Demonstration of printing performances

Our all-in-cryogenic procedure enables high-resolution high-aspect-ratio 3D-architectured hydrogels. This capability is achieved by instant solidification (< 0.5 s, one order faster than previously reported strategies[35,36] in Supplementary Fig. 9 and Supplementary Note 4). We further demonstrate the improved resolution of MCP technique compared to room-temperature printing on a variety of printing kinetic conditions (like ink rheology and substrates) but no significant property degradations (Fig. 2e and Supplementary Fig. 10). With the MCP technique, we eliminate the capillarity-driven instability and improve the printing resolution, i.e., minimum linewidth in the X-Y plane, to about 42 μm (Supplementary Fig. 11a). The viscosity range of printable inks extends from 1.09 to 2332.69 Pa s at the shear rate of $0.1 \, s^{-1}$ (Supplementary Fig. 12), covering most conventional DIW techniques[17]. Fine temperature control further promises subvoxel engineering, including pore morphology and phase separation (Supplementary Fig. 13, 14). Notably, due to the mechanical limitation of our cryogenic platform and DIW printer, the maximum printable size of our hydrogel structures is about 40 mm × 40 mm × 20 mm (Supplementary Fig. 2, 11), which can be expandable by the configuration design of cryogenic fields.

We next validate the multimaterial printing performance across hydrogel materials that have varying forming mechanisms (Supplementary Fig. 15). The uniaxial tensile tests of printed heterogeneous hydrogels show that each hybrid sample fractures at the composed homogenous hydrogel itself, rather than debonds at the junction part (Fig. 2i). Further fatigue and long-term cyclic tests exhibit rival fatigue thresholds at both homogenous and heterogeneous hydrogels, confirming the robust interfaces within our printed architectures (Supplementary Fig. 16).

By regulating the cryogenic printing parameters and cross-linking kinetics, we can further finely tune the mechanical properties of multimaterial hydrogel structures (Supplementary Fig. 7d). Figure 2j shows a wide printable range of Young's modulus Y (3.72–153.56 kPa) in our printed PVA hydrogel samples. By introducing the index of mechanical tunability (defined as Y_{max}/Y_{min}) and extreme aspect ratio (the ratio of structure height to resolution), our MCP demonstrates a combination of wide-range tunability (> 41) and high aspect ratio features (> 476) (Fig. 2j and Supplementary Table 1)[10,12–14,22,37–46].

Multimaterial 3D hydrogel architectures

To highlight this fabrication capability, we design a series of architectures with increasing geometrical complexity. First, we show the facile fabrication of typical freestanding 3D structure elements, such as overhanging Sierpinski pyramids, thin-walled Y-shape tubes, and hollow cubes (Fig. 3a–c). By altering material choices, versatile hydrogel components and their integration can be employed to constitute sophisticated heterogeneous architectures with functionalities. We exemplify a range of multimaterial 3D hydrogel structures, including voxelated digital cubes, in-tube stents, and lattice metamaterials (Fig. 3d–f and Supplementary Video 2). The fabricated structures show mechanical robustness against deformations like stretching, pressing, and twisting (Fig. 2i, Fig. 3g–i, and Supplementary Fig. 16), providing excellent reliability and durability for soft robotic applications.

We further use an X-ray computed tomography (XCT) to evaluate the shape fidelity of printed hydrogel structures (Fig. 3j–l). Exemplified by a multimaterial primitive lattice (Fig. 3f), horizontal and vertical XCT scanning slices show a high-fidelity hollow heterogeneous structure with consistent submillimeter-thickness walls (Fig. 3j). Quantitative comparison using the XCT reconstruction reveals an accurate match with the original design model (68.3% of the printed surface locations lie within 227 μm of their desired locations, and 95.4% lie within 428 μm, Fig. 3k, l).

All-printed all-hydrogel soft machines

To further harness the advantages of our MCP technique, we showcase the manufacturing of various all-hydrogel bioelectronics and soft machines with enriched functionalities and extended capabilities.

For bioelectronic prototypes, we design and fabricate an all-hydrogel biomimetic aortic heart valve with leaflet-status perception by integrating poly(3,4-ethylenedioxythiophene):poly(styrene sulfonate)-poly(vinyl alcohol) (PEDOT:PSS-PVA) conductive chamber with PVA leaflets (Fig. 4a). The printed valve displays a size comparable to that of a native teenager heart valve, and the surface profile error is less than 6% with a maximum surface inclination of 43.7° (Fig. 4b). During the simulated systolic and diastolic cycles, the leaflets compliantly respond to the transvalvular flows and induce the variations of chamber pressure. These fluctuations further reflect on the resistance of the PEDOT:PSS-PVA hydrogel, showing a great linearity ($R^2 = 0.99$) with varying leaflet displacement (Fig. 4c and Supplementary Fig. 17). The resistance response in pulse flow cycles also exhibits a low hysteresis (~ 8.3%) under wide-range inlet hydrodynamic pressure (−11.7 to 12.8 kPa) (Supplementary Note 5). Further periodic square-wave flow tests demonstrate that the resistance response can follow the leaflet displacement with repetitive and stable output signals (Fig. 4d and Supplementary Video 3). The experimental observation validates that the applied maximum hydrodynamic pressure can exceed 140 mmHg, covering the normal range of native aortic blood pressure.

To further demonstrate multifunctional soft machines, we continuously print multiple material components to implement the untethered multimode magnetic turbine robot with tailorable sizes (typically ~12.5 mm diameter) (Fig. 5a and Supplementary Video 4). This turbine-like magnetic robot consists of a magnetic platform and twenty soft-hard composite blades. By applying a magnetic field **B**, the magnetic platform (with a volume V and an in-plane magnetization **M**) generates a torque regulated by $\mathbf{T} = V(\mathbf{M} \times \mathbf{B})$, which causes the rotation of itself and on-platform blades to align its magnetization with the magnetic field (Fig. 1c). This rotary motion enables soft-hard composite blades to sweep obstacles, where soft blades can compliantly
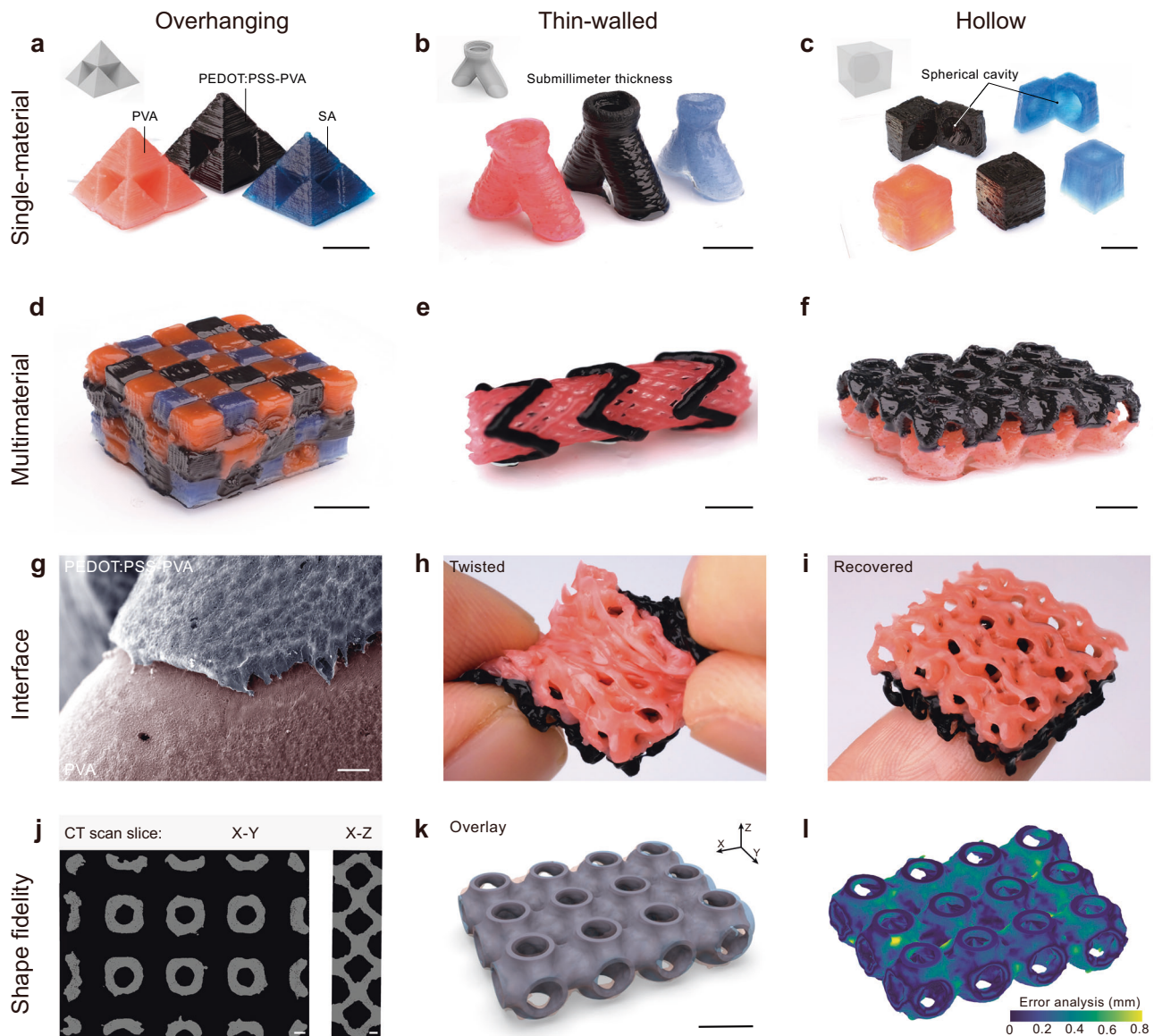
Fig. 3 | Characterizations of printed structures. a–c Single-material structures: **a** Sierpinski pyramids. **b** Y-shape tubes. **c** Hollow cubes with a spherical cavity. **d–f** Multimaterial structures: **d** Voxelated digital cube. **e** Cylindrical in-tube stent. **f** Primitive lattice. **g–i** Material interface in a printed hydrogel gyroid lattice: **g** SEM images of material interfaces between PEDOT:PSS-PVA and PVA show a tightly bonding morphology. **h** The soft printed hydrogel withstands twisting deformation. **i** The printed hydrogel recovers to its original shape after twisting, illustrating mechanical robustness. **j–l** Shape fidelity in a printed hydrogel primitive lattice: **j** X-ray computed tomography (CT) scanning slices demonstrate a uniform structure array with thin-walled (<1 mm), overhanging, and hollow features: Horizontal (X-Y plane) and vertical (X-Z plane). **k, l** The printed structure overlays well with the designed model, and quantitative error analysis shows agreement between the two models (428 µm error range corresponds to 95.4% of all points). To distinguish different materials, the printed hydrogels are composed of pigments: PVA (red) and SA (blue). Scale bars, 5 mm (**a**–**f**), 20 µm (**g**), 1 mm (**j**), 5 mm (**k**).

anchor the target location, and hard parts generate dredging torque and propulsion force. This composite blade design is also capable of dragging motion by generating a trapping vortex behind the rotating swimming robot (Fig. 1c). The finite element analysis in Fig. 5b exhibits a typical flow field around the turbine robot in an underwater pipe, where the inlet water flow develops under the robot's disturbance and forms a cone-like trapping vortex (marked in gray color). Such a flow field enables the robot to trap floating objects inside the vortex region and drag them for transportation (Fig. 5c). Thus, the designed untethered turbine robot possesses two locomotion modes: sweeping with rotating blades and dragging by the trapping vortex (Fig. 1d). We can reverse the rotational axis direction of the magnetic field to flip the turbine robot (facing with or facing away from the target object) for locomotion mode switching in tasks (Fig. 5d, e). By controlling a rotary bar magnet (5–10 mT at ~400 rpm speed), we demonstrate that this turbine robot can provide about 0.1 N dredging force to remove sticky blockages underwater in straight tubes and trap floating obstacles to avoid blockage migration (Fig. 5d and Supplementary Video 5). In a more complicated Y-shape tube, our turbine robot can transport a capsular-like cargo (~0.35 g weight) by steering its rotational axis within half a minute (Fig. 5e and Supplementary Video 6).

Discussion

In this study, we propose a multimaterial cryogenic printing technique harnessing an all-in-cryogenic solvent phase transition strategy for generalized 3D hydrogel fabrication. Our technical platform presents the capability on material diversity and geometrical complexity for constructing multimaterial 3D hydrogel architectures. Our
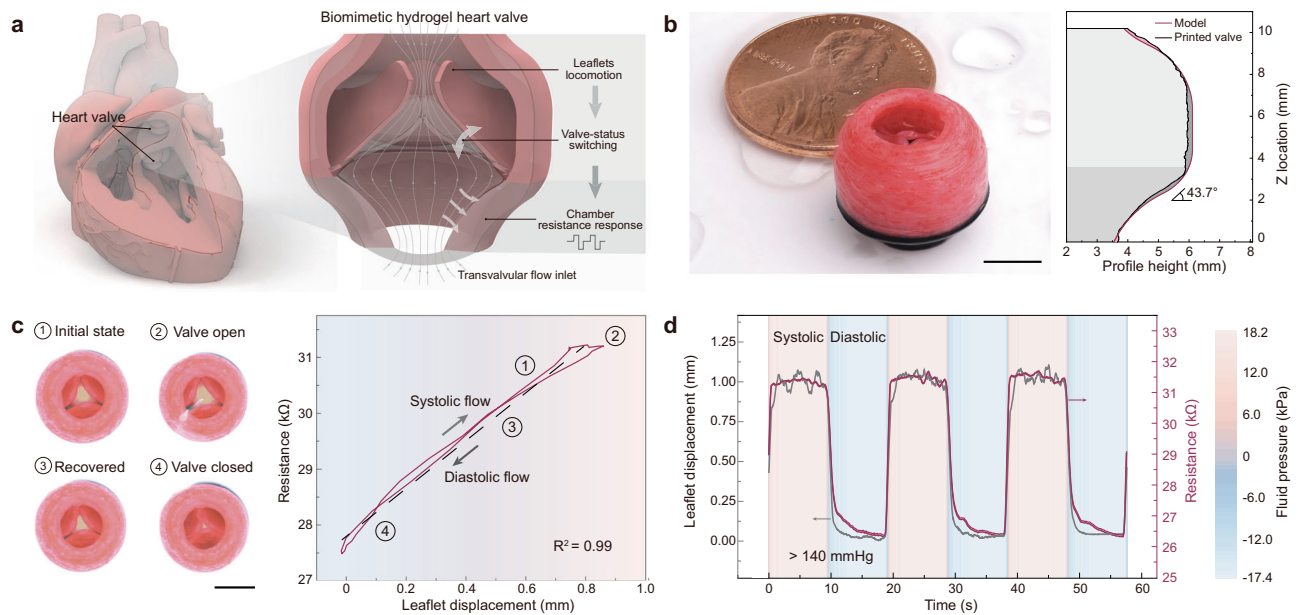
Fig. 4 | Self-sensing biomimetic heart valve. a Schematic diagram of a biomimetic hydrogel heart valve: Flow-response leaflets and induced PEDOT:PSS-PVA chamber signal sensing. **b** Photograph of printed hydrogel heart valve and surface profile analysis. Its profile error is less than 6% with a maximum surface inclination of 43.7°. **c** Photograph of typical operation statuses of the hydrogel heart valve and corresponding loading and unloading resistance responses, exhibiting a great linearity $R^2 = 0.99$ under simulating fluid pressure (−11.7 to 12.8 kPa). **d** Loading and unloading resistance responses under periodic square-wave flow show timely, repetitive, and stable signals following the leaflet displacement. This self-sensing valve can withstand extreme hydrodynamic pressure (> 140 mmHg), covering the normal range of native aortic blood pressure. Scale bars, 5 mm.

demonstrations on all-printed all-hydrogel soft machines explore broad prospects in soft robotics and biomedical electronics.

Methods

Materials

Agents: Poly(3,4-ethylenedioxythiophene):poly(styrene sulfonate) (PEDOT:PSS) nanofibrils (Orgacon Dry) was purchased from Agfa Materials. Poly(vinyl alcohol) (PVA, $Mw = 146{,}000-186{,}000$, >99% hydrolyzed) was purchased from Sigma-Aldrich. Sodium alginate (SA, AR, viscosity 200 ± 20 mPa s), chitosan ($\geq 95\%$ deacetylated, viscosity 100–200 mPa s), calcium chloride ($CaCl_2$, $\geq 96\%$), and dimethyl sulfoxide (DMSO, $\geq 99\%$) were purchased from Aladdin Reagent Co., Ltd (Shanghai, China). Glutaraldehyde (GA, 25% in H_2O) was purchased from Macklin Biochemical Technology Co., Ltd (Shanghai, China). Neodymium-iron-boron (NdFeB) powders (~5 μm in size) were purchased from Magnequench Co. Ltd. Water-soluble pigments were purchased from AmeriColor Corp., and lipid-soluble pigments were purchased from Facai Technology Co., Ltd (Ji'nan, China). Printing nozzles: 200- and 100-μm nozzles were purchased from Nordson EFD and 60-μm nozzles from World Precision Instruments. All the chemicals were used without further purification.

Preparation of printable hydrogel inks

To prepare SA inks, SA powders were dispersed in deionized (DI) water with a mass ratio of 4%, and then stirred until completely dissolved. For PVA hydrogel inks, PVA particles were added to DI water and stirred at 90 °C until completely dissolved. To fabricate soft-hard composite blades in the turbine robots, 10 wt.% and 11.5 wt.% PVA inks are prepared for soft blades and hard blades, respectively. The PVA-NdFeB inks were prepared by mixing 10 wt.% NdFeB particles into 12.5% PVA inks for the magnetic platform in the robots. To prepare chitosan inks, 0.5 g of chitosan was dissolved in 9.5 g of dilute hydrochloric acid (1 M) and stirred until completely dissolved. PEDOT:PSS nanofibrils were re-dispersed with a DI water-DMSO mixture (85:15 v/v) and filtered with a syringe filter (30 μm) at room temperature. PEDOT:PSS solution and PVA ink were thoroughly mixed with a syringe filter (30 μm) to prepare PEDOT:PSS-PVA inks, and the mass ratio of 7% PEDOT:PSS solution to 7% PVA solution is 2:3.

Preparation of cross-linking baths

Cross-linking baths were first prepared by mixing DI water with anhydrous ethanol (70:30 v/v). To prepare baths for physical cross-linking, 2 g calcium chloride particles were dissolved and stirred until completely dissolved. As for chemical cross-linking baths, GA and hydrochloric acid were mixed into the above ethanol-aqueous solution with concentrations of 0.054 M and 0.1 M, respectively. All the cross-linking baths were stirred for 2 h and cooled to reaction temperature before use.

Cryogenic printing procedure

The printing procedure was conducted by using a custom-made DIW-based 3D printer, including a Z-axis linear rail as well as an X- and Y-axis movement platform equipped with a Peltier plate (TP102, Instec Inc.). Hydrogel inks were housed in a syringe (10 mL, EFD Inc.), which was Luer-locked to the nozzles, and extruded by the air pressure generated by a fluid dispenser (Ultimus V, EFD Inc.). Printhead trajectories were generated either by custom-writing or using an open-source software Cura to convert designed 3D models (STL files) into G-code to digitally control the relative motion between the printhead and the movement platform. The Peltier plate was set at a constant or stepwise reducing temperature considering specific structures (Supplementary Fig. 13 and Note 6).

Cryogenic cross-linking

The cross-linking procedure involves the immersion of printed structures in the prepared cross-linking bath. The duration time was typically 12 h, and the reaction was conducted under −5 °C unless otherwise noted (See Supplementary Note 6 for details). After cross-
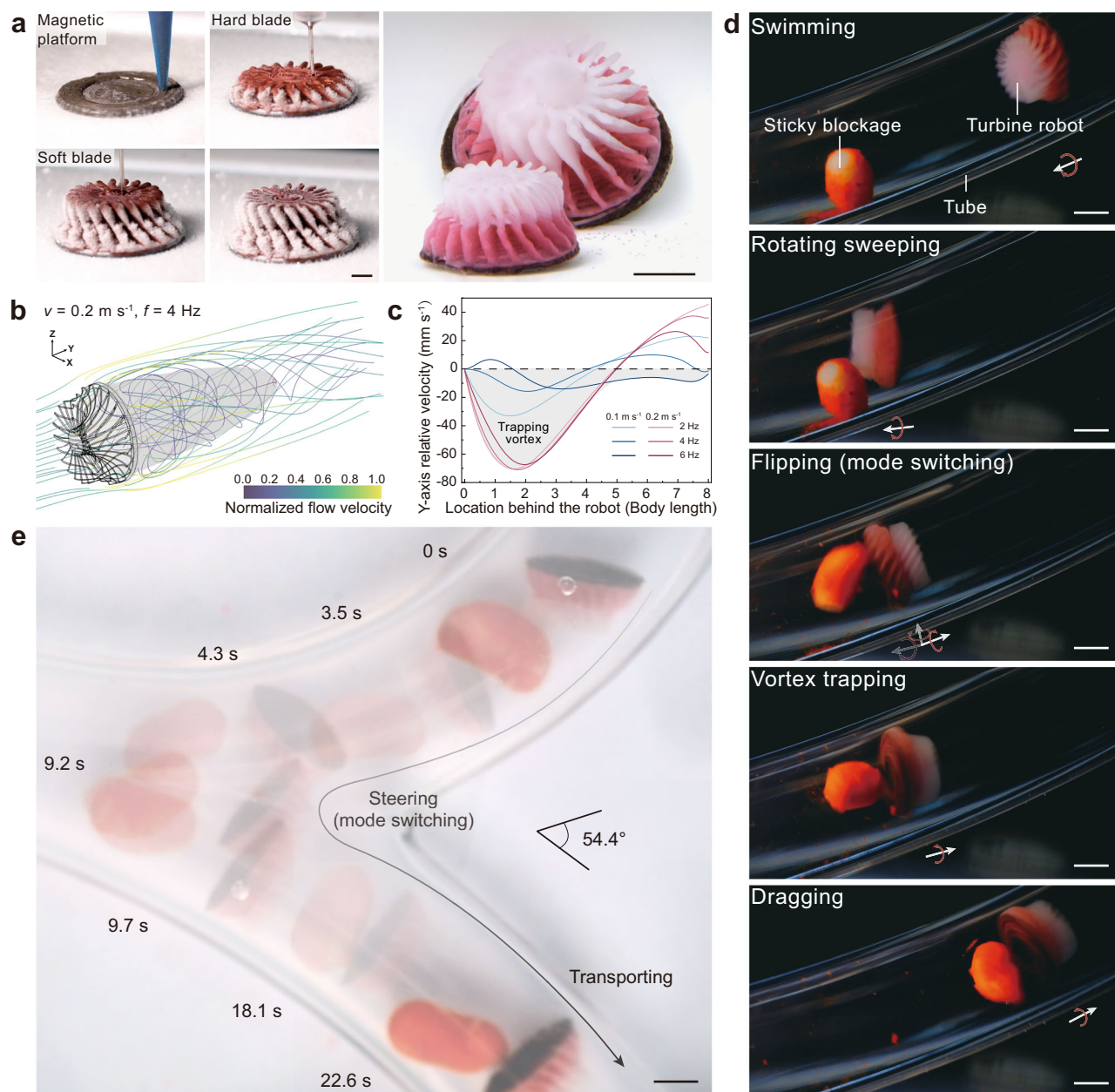
Fig. 5 | Untethered multimode magnetic turbine robot. a Photograph of continuously printing the turbine robot into customized sizes (typically ~12.5 mm diameter and ~5.4 mm height). **b** The simulation analysis of a typical flow field around the rotating swimming turbine robot in an underwater pipe with a diameter of 20 mm. The trapping vortex behind the robot is marked in gray color, where the vector direction of the Y-axis component velocity is opposed to the Y direction. v, swimming speed; f, rotating frequency. **c** The relative velocity component in the Y direction of trapped objects to the robot under varying swimming speeds and rotating frequencies. **d** The removal process of sticky blockages in an underwater straight tube by using the turbine robot to trap floating obstacles and avoid blockage migration. Typical processes include: Swimming to the target location, rotating sweeping, flipping (mode switching), vortex trapping, and dragging for removal. The propulsion and rotation directions of the robot are marked in white and brown, respectively. **e** The multimode turbine robot transports a capsular-like cargo through a Y-shape tube by steering its rotational axis. The angle between the front and rear paths is about 125.6°. Scale bars, 5 mm.

linking, printed hydrogels were washed with DI water at 5 °C for several times to remove excessive agents and then swollen for 24 h to achieve the equivalent state.

Rheological characterizations
The characterizations were conducted by using a controlled stress rheometer (Discovery HR 20, TA Instruments). Ink viscosities were measured as a function of shear rate from 0.1 to 100 s⁻¹. Three-interval thixotropy test for rheological recovery was conducted at 10 rad s⁻¹.

Mechanical characterizations
All mechanical characterizations were performed by using the fully swollen hydrogel samples in DI water. Uniaxial tensile tests were measured by a universal mechanical testing equipment (Instron 68SC-2, USA) at a constant crosshead speed of 36 mm min⁻¹. For the calculation of Young's modulus, strains from 1 to 10% were used as the stress-strain response in this region was linear. The fatigue threshold and cyclic stability were performed with fully swollen hydrogels immersed in a water bath to prevent the dehydration-induced crack propagation (See Supplementary Note 7 for details).

Electrical characterization

The resistance signal of the PEDOT:PSS-PVA chamber sensor was measured by a precise LCR (inductance-capacitance-resistance) meter (E4980AL, Keysight Technologies Inc.).

Optical observation

In-situ observations of printed filaments and structures were imaged by an optical microscope (ZWSP-4KZD). The corresponding sizes were measured and analyzed with Fiji software. Profiles of printed structures were analyzed by an ultra-depth three-dimensional microscope (VHX-7000, Keyence Corp.).

Scanning electron microscopy (SEM)

The fully-swollen hydrogels were immersed in liquid nitrogen for 3 min. Then, frozen samples were freeze-dried under vacuum conditions of 8×10^{-2} Torr and fractured to obtain a clean cross-section. The samples were characterized by using a scanning electron microscope (Gemini 360, Zeiss, Germany) with 5 nm Pt sputtering to enhance image contrasts. Energy dispersive spectroscopy mapping was imaged to analyze the multimaterial hydrogel interfaces by sulfur and calcium elements.

Raman spectra

Raman spectra were employed to characterize the cross-linking reaction by combination with a Peltier plate for cryogenic conditions. An inVia confocal Raman microscope (Renishaw Inc.) was used with a laser excitation wavelength of 785 nm with an output of 100 mW power.

Differential scanning calorimetry (DSC)

The phase transition behavior of hydrogel inks and cross-linking baths were analyzed by using a differential scanning calorimeter (DSC2500, TA Instruments). Dynamic heating scans were conducted from 20 to $-30\,°C$ and then back to $20\,°C$ at a heating rate of $1\,°C$ min^{-1} for baths and $5\,°C$ min^{-1} for hydrogel inks in a nitrogen atmosphere.

Atomic force microscope phase imaging

Atomic force microscope (AFM) phase images of the lyophilized hydrogel samples were acquired by an AFM (MFP-3D, Asylum Research).

X-ray computed tomography (XCT)

The primitive lattice was printed, cross-linked, swollen, and imaged by using an Xradia 520 Versa CT scanner (Zeiss, Germany). The reconstruction was conducted by using the software Dragonfly.

Computational fluid dynamics simulations

Simulation analyses were conducted by using the COMSOL Multiphysics software (v. 6.2). The flow-field simulation was carried out by using the k-ε turbulence model and moving mesh in the fluid flow module. The detailed simulation setup and parameters can be found in Supplementary Note 8.

Data availability

All data needed to evaluate the conclusions are presented in the paper, its Methods, and Supplementary Information. The original videos and data are available from the corresponding authors on request. The source data for Figs. 2c-e, 2g-i, 4b-d, 5c, and Supplementary Figs. 6, 7d, 8, 10, 12, 13d, 16b are provided as a separate Source Data file. Source data are provided with this paper.

References

1. Dobashi, Y. et al. Piezoionic mechanoreceptors: force-induced current generation in hydrogels. *Science* **376**, 502–507 (2022).
2. Dong, E. et al. Bioinspired metagel with broadband tunable impedance matching. *Sci. Adv.* **6**, eabb3641 (2020).
3. Yi, J. et al. Water-responsive supercontractile polymer films for bioelectronic interfaces. *Nature* **624**, 295–302 (2023).
4. Zhao, Y. et al. A self-healing electrically conductive organogel composite. *Nat. Electron.* **6**, 206–215 (2023).
5. Xu, P. et al. Conductive and elastic bottlebrush elastomers for ultrasoft electronics. *Nat. Commun.* **14**, 623 (2023).
6. Wang, C. et al. Bioadhesive ultrasound for long-term continuous imaging of diverse organs. *Science* **377**, 517–523 (2022).
7. Koffler, J. et al. Biomimetic 3D-printed scaffolds for spinal cord injury repair. *Nat. Med.* **25**, 263–269 (2019).
8. Wang, T. et al. A chemically mediated artificial neuron. *Nat. Electron.* **5**, 586–595 (2022).
9. Kam, D., Rulf, O., Reisinger, A., Lieberman, R. & Magdassi, S. 3D printing by stereolithography using thermal initiators. *Nat. Commun.* **15**, 2285 (2024).
10. Ge, Q. et al. 3D printing of highly stretchable hydrogel with diverse UV curable polymers. *Sci. Adv.* **7**, eaba4261 (2021).
11. Cheng, J. et al. Centrifugal multimaterial 3D printing of multifunctional heterogeneous objects. *Nat. Commun.* **13**, 7931 (2022).
12. Choi, S. et al. Fibre-infused gel scaffolds guide cardiomyocyte alignment in 3D-printed ventricles. *Nat. Mater.* **22**, 1039–1046 (2023).
13. Hui, Y. et al. Three-dimensional printing of soft hydrogel electronics. *Nat. Electron.* **5**, 893–903 (2022).
14. Xie, X. et al. Liquid-in-liquid printing of 3D and mechanically tunable conductive hydrogels. *Nat. Commun.* **14**, 4289 (2023).
15. Chen, F. et al. Phase-separation facilitated one-step fabrication of multiscale heterogeneous two-aqueous-phase gel. *Nat. Commun.* **14**, 2793 (2023).
16. Won, D. et al. Digital selective transformation and patterning of highly conductive hydrogel bioelectronics by laser-induced phase separation. *Sci. Adv.* **8**, eabo3209 (2022).
17. Li, J., Cao, J., Lu, B. & Gu, G. 3D-printed PEDOT:PSS for soft robotics. *Nat. Rev. Mater.* **8**, 604–622 (2023).
18. Li, X. & Gong, J. P. Design principles for strong and tough hydrogels. *Nat. Rev. Mater.* **9**, 380–398 (2024).
19. Qu, S. 3D printing of hydrogel electronics. *Nat. Electron.* **5**, 838–839 (2022).
20. Lou, L., Bilbao-Sainz, C., Wood, D. & Rubinsky, B. Temperature controlled cryoprinting of food for dysphagia patients. *Innovative Food Sci. Emerg. Technol.* **86**, 103362 (2023).
21. Zhang, W., Leu, M. C., Ji, Z. & Yan, Y. Rapid freezing prototyping with water. *Mater. Des.* **20**, 139–145 (1999).
22. Tan, Z., Parisi, C., Di Silvio, L., Dini, D. & Forte, A. E. Cryogenic 3D printing of super soft hydrogels. *Sci. Rep.* **7**, 16293 (2017).
23. Li, Z., Xu, M., Wang, J. & Zhang, F. Recent advances in cryogenic 3D printing technologies. *Adv. Eng. Mater.* **24**, 2200245 (2022).
24. Adamkiewicz, M. & Rubinsky, B. Cryogenic 3D printing for tissue engineering. *Cryobiology* **71**, 518–521 (2015).
25. Warburton, L. & Rubinsky, B. Cryopreservation of 3D bioprinted scaffolds with temperature-controlled-cryoprinting. *Gels* **9**, 502 (2023).
26. Warburton, L., Lou, L. & Rubinsky, B. A modular three-dimensional bioprinter for printing porous scaffolds for tissue engineering. *J. Heat. Transf.* **144**, 031205 (2022).
27. Rubinsky, B. & Ikeda, M. A cryomicroscope using directional solidification for the controlled freezing of biological material. *Cryobiology* **22**, 55–68 (1985).
28. Lou, L. & Rubinsky, B. Temperature-controlled 3D cryoprinting inks made of mixtures of alginate and agar. *Gels* **9**, 689 (2023).
29. Warburton, L. & Rubinsky, B. Freezing-modulated-crosslinking: a crosslinking approach for 3D cryoprinting. *Bioprinting* **27**, e00225 (2022).

30. Kalita, A. et al. Microstructure and crystal order during freezing of supercooled water drops. *Nature* **620**, 557–561 (2023).
31. Zawada, B., Ukpai, G., Powell-Palm, M. J. & Rubinsky, B. Multi-layer cryolithography for additive manufacturing. *Prog. Addit. Manuf.* **3**, 245–255 (2018).
32. Hong, J. et al. Imaging surface structure and premelting of ice Ih with atomic resolution. *Nature* **630**, 375–380 (2024).
33. Wettlaufer, J. S. & Worster, M. G. Premelting dynamics. *Annu. Rev. Fluid Mech.* **38**, 427–452 (2006).
34. Dodda, J. M. et al. Comparative study of PVA/SiO_2 and $PVA/SiO_2/$ glutaraldehyde (GA) nanocomposite membranes prepared by single-step solution casting method. *J. Mater. Sci.* **50**, 6477–6490 (2015).
35. Pawar, A. A. et al. High-performance 3D printing of hydrogels by water-dispersible photoinitiator nanoparticles. *Sci. Adv.* **2**, e1501381 (2016).
36. Slesha Tuladhar C. N., Ahasan Habib. Rheological study of highly thixotropic hydrogels for 3D bioprinting processes. In: *Proceedings of the 2021 IISE Annual Conference)* (2021).
37. Xie, R. et al. Magnetically driven formation of 3D freestanding soft bioscaffolds. *Sci. Adv.* **10**, eadl1549 (2024).
38. Xin, S. et al. Generalizing hydrogel microparticles into a new class of bioinks for extrusion bioprinting. *Sci. Adv.* **7**, eabk3087 (2021).
39. Williams, A. H. et al. Printable homocomposite hydrogels with synergistically reinforced molecular-colloidal networks. *Nat. Commun.* **12**, 2834 (2021).
40. Wei, H. et al. Orthogonal photochemistry-assisted printing of 3D tough and stretchable conductive hydrogels. *Nat. Commun.* **12**, 2082 (2021).
41. Ouyang, L. et al. Expanding and optimizing 3D bioprinting capabilities using complementary network bioinks. *Sci. Adv.* **6**, eabc5529 (2020).
42. Caprioli, M. et al. 3D-printed self-healing hydrogels via digital light processing. *Nat. Commun.* **12**, 2462 (2021).
43. Zhou, X. et al. Photoinduced double hydrogen-atom transfer for polymerization and 3D printing of conductive polymer. *Nat. Synth.* **3**, 1145–1157 (2024).
44. Honaryar, H., LaNasa, J. A., Lloyd, E. C., Hickey, R. J. & Niroobakhsh, Z. Fabricating robust constructs with internal phase nanostructures via liquid-in-liquid 3D printing. *Macromol. Rapid Commun.* **42**, 2100445 (2021).
45. Mishra, A. K. et al. Autonomic perspiration in 3D-printed hydrogel actuators. *Sci. Robot.* **5**, eaaz3918 (2020).
46. Shoushtari Zadeh Naseri, A. et al. A novel cryogenic approach to 3D printing cytocompatible, conductive, hydrogel-based inks. *3D Print. Addit. Manuf.* **11**, 447–459 (2024).

Acknowledgements

Author contributions

G.G., B.L., X.Z., and J.L. guided the whole research project. G.G., B.L., and J.L. conceived the research. J.L. designed the techniques and conducted analysis and characterizations. J.L. and J.C. performed crosslinking characterizations. J.L. and R.W. conducted experiments on mechanical properties. J.L. and R.B. carried out evaluations on biomimetic heart valves. J.L. and J.C. prepared figures with input from all authors. G.G., B.L., X.Z., and J.L. wrote the manuscript with input from all authors. All authors participated in drafting the manuscript and interpreting the data.

Competing interests

G.G. and J.L. are co-applicants of a pending patent (application number CN202411841590.0, filed 13 December 2024) related to the technology used in this study and filed at the China National Intellectual Property Administration. The other authors declare no competing interests.

Additional information

Supplementary information The online version contains supplementary material available at https://doi.org/10.1038/s41467-024-55323-6.

Correspondence and requests for materials should be addressed to Xiangyang Zhu, Baoyang Lu or Guoying Gu.

Peer review information *Nature Communications* thanks the anonymous reviewers for their contribution to the peer review of this work. A peer review file is available.

Reprints and permissions information is available at http://www.nature.com/reprints

Publisher's note Springer Nature remains neutral with regard to jurisdictional claims in published maps and institutional affiliations.